ARTICLE   OPEN

Check for updates

Self-cross-linked arrays enabled flexible mechanical sensors for monitoring the body tremor

Xuewen Wang [1,2,10 ✉], Wei Fu [3,10], Guanhui Gao[4], Mandeep Singh Mehay[5], Lu Zheng[1,2,6], Hong Wang[5], Wu Zhao[7], Kian Ping Loh[3], Ting Zhang[8], Wei Huang[1,2] and Zheng Liu [5,9 ✉]

Thin-film electronics played an important role in flexible healthcare sensor applications. The common status of their constituent blocks are solid film and network structures. However, the solid film could only sustain bend in a narrow range due to cracks, and the network structure decreased the sensitivity of flexion sensors due to the strong interactions between nanowires. New materials and technologies are urgently required for flexible sensing electronics, to produce the reliable data for assessment of the human body. Here, we report on a novel three-dimensional (3D) carbon nanorods array (CNA) that is characterized as vertically aligned nanorods and self-cross-linked junctions. We also demonstrate the CNA-based flexible healthcare sensors in monitoring the Parkinsonian tremors. Comparing with two-dimensional (2D) carbon nanotube networks and solid thin films, such self-cross-linked geometries are highly resistant to crack and fragmentation under strain. In the meantime, it shows high sensitivity and good stability (~10,000 times) to detect the flexions. These CNA-based flexible devices are capable of recording low-frequency vibrations (<6 Hz) and make it excellent to monitor the rest tremor of the human body, which is an initial symptom of Parkinson's disease. The 3D self-cross-linked CNA film shows great potential in the fabrication of cost-effective and durable flexible sensors for early diagnosis of disease by monitoring the health-related rest tremors.

npj Flexible Electronics (2020)4:8 ; https://doi.org/10.1038/s41528-020-0071-3

INTRODUCTION

Thin-film electronics are dominant configurations for current flexible sensing electronics, such as flexible pressure and strain sensors[1–3]. The most important benefit of the thin film is easy micro-manufacturing for large-scale integrations, because it is compatible with traditional micro-processing technology[3–6]. Recent studies have demonstrated several thin-film flexible/stretchable electronics based on flat solid thin film and micro-structured thin film with wrinkles and nanowire network[7–10]. Typically, the flat solid thin film requires the materials should be intrinsic stretchable and flexible, such as polymers and elastic rubbers. However, the solid film by rigid inorganic material is challenging to be used in flexible electronic applications because the stress in the film could produce cracks and fragmentations under large strain (Fig. 1). By structural engineering, two-dimensional (2D) networks have been developed for improving the flexibility of films, which constitute of nanowires and nanotubes by wet chemical assembly process and chemical vapor deposition (CVD) growth with the dry transfer. However, most of the contact points between the nanowires/nanotubes are only bonded physically, resulting in contact resistance at the interface and, in turn, casting a shadow on the electrical stability and reliability of the material upon repeated bending and when used in flexible electronics[11]. To eliminate the negative influence of contact resistance, scientists have developed aligning and welding methods to reduce the contact points and contact resistance of network films[12–15]. However, it is difficult to keep a balance between sensitivity and stability because there needs a suitable ratio of physical bonds and chemical bonds in network film. Here, we demonstrated a novel film of 3D self-cross-linked array that contains both physical bond and chemical bond. This unique 3D configuration in film enabled the film with large structural deformation under strain and bend, and improve the flexibility and sensitivity for flexible sensing applications.

Current studies have established the carbon-based nanomaterials (e.g., CNT and graphene) as great candidates for flexible mechanical sensors, such as flexible pressure and strain sensors[16–19]. These flexible sensors have shown their capabilities in monitoring the health-related physiological signals, such as heart rate, blood pressure, and wrist pulse[17,20,21]. Therefore, flexible sensors can be used for wearable health monitoring, which is a convenient and noninvasive way for disease pre-diagnosis and health assessment. However, most of the current flexible sensors are limited to track cardiovascular and blood diseases. To the best of our knowledge, the monitoring of Parkinsonian tremor by flexible/wearable sensors is quite rare, although Parkinson's disease is vastly prevalent in the current aging society[22]. In this work, we have synthesized 3D self-cross-linked carbon arrays (CNA) and subsequently fabricated flexible sensing electronics for the detection of Parkinsonian tremor. We have found that the 3D self-cross-linked CNA is composed of an individual carbon nanorod, which is an "intermediate" form between the carbon nanotube and carbon

[1]Frontiers Science Center for Flexible Electronics (FSCFE) & Shaanxi Institute of Flexible Electronics (SIFE), Northwestern Polytechnical University, 127 West Youyi Road, Xi'an 710072, China. [2]MIIT Key Laboratory of Flexible Electronics (KLoFE), Northwestern Polytechnical University, 127 West Youyi Road, Xi'an 710072, China. [3]Department of Chemistry and Centre for Advanced 2D Materials, National University of Singapore, 3 Science Drive 3, 117543 Singapore, Singapore. [4]Paul-Drude-Institut für Festkörperelektronik, Leibniz-Institut im Forschungsverbund Berlin, Hausvogteiplatz 5-7, Berlin 10117, Germany. [5]School of Materials Science and Engineering, Nanyang Technological University, 50 Nanyang Avenue, Singapore 640260, Singapore. [6]Institute of Biomedical Materials and Engineering (IBME), Northwestern Polytechnical University, 127 West Youyi Road, Xi'an 710072, China. [7]School of Information Science and Technology, Northwest University, Xi'an 710069, China. [8]i-Lab, Suzhou Institute of Nano-Tech and Nano-Bionics, Chinese Academy of Sciences, Suzhou 215123, China. [9]Centre for Micro-/Nano-electronics (NOVITAS), School of Electrical and Electronic Engineering, Nanyang Technological University, Singapore 639798, Singapore. [10]These authors contributed equally: Xuewen Wang, Wei Fu. ✉email: iamxwwang@nwpu.edu.cn; z.liu@ntu.edu.sg
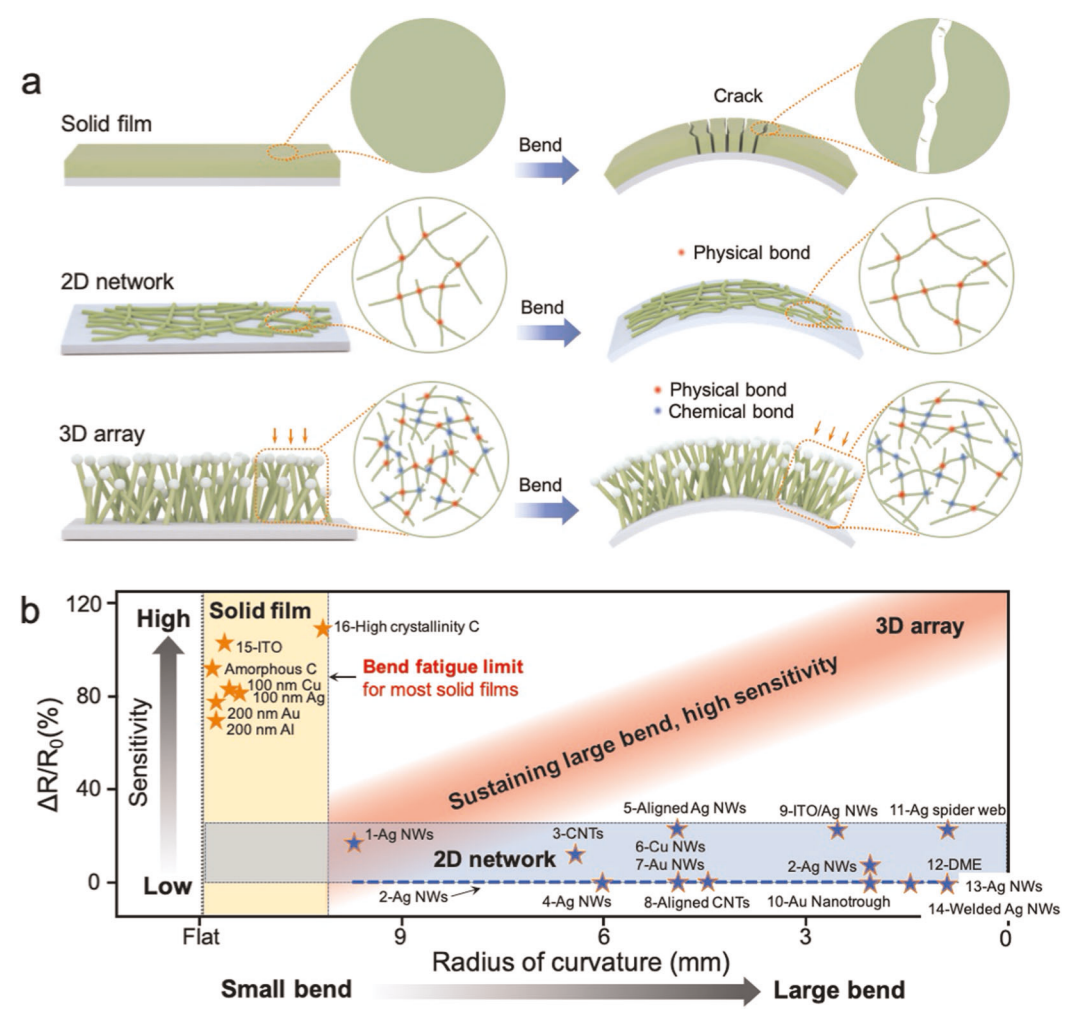
Fig. 1 Film-based flexible electronics and their performance. a Schematic illustrations of solid film, 2D networks, and 3D array-based films under bend. **b** Summary of the sensitivity with bend ratios from film-based flexible electronics. (References could be find from the Supplementary Information).

nanofiber. The self-cross-linked structure enhances the contact points between individual carbon nanorod units, and eradicates the electrical instability by reducing the residual stresses in the material. Our CNA-based flexible sensors exhibit high sensitivity and good stability (~10,000 times) in the detection of flexions and low-frequency vibrations (<6 Hz), and show great potential in pre-screening of Parkinsonian's disease.

RESULTS

Characterization of carbon nanorod arrays

The self-cross-linked CNA was synthesized by CVD method at high temperatures (~1000 °C) and dynamic change of pressure, using CH_4 as the carbon precursor. In the growth process, the pressure is dynamically changed within the range of ~1.5 to ~160 m bar by controlling the amount of reaction gases added. The 5-nm Ni film on SiO_2/Si substrate was used as a catalyst to grow CNA because the Ni has a great ability to dissolve carbon, and it has been proven as a good catalyst for the growth of CNT[23–26]. In this experiment, the pressure change is the crucial parameter to ensure the production of CNA instead of CNT. As displayed in Fig. 2a, the self-cross-linked CNA is a microstructured thin film, and it composes of carbon nanorods (CNRs) which are terminated by Ni/C particles and cross-linked to each other to form the thin film. The interlaced points between individual carbon materials serve

as an electronic channel that permits electrical conductivity. The CNR has a different structure as compared with CNT. Figure 2b schematically illustrates the cross-section simulation of CNR. There are two characteristics that distinguish the CNR from CNT: (i) the solid and layered carbon atom packing (without inner hollow and tubular structure like CNT); (ii) the carbon layer that tightly covers the whole Ni catalyst different from the partial cavity at the outside of the Ni catalyst in the CNT (see Supplementary Figs. S1, S2). The photographs and top-view SEM images indicate that we have synthesized large-scaled, uniformed, and high-quality CNA (Fig. 2c; Supplementary Fig. S3). The side view SEM image shows the length/diameter (L/D) ratio of the CNRs to be around 10. It also shows that the CNRs are approximately vertical and incline to the substrate (Fig. 2d), and are self-cross-linked. In this method, the L/D ratio of CNRs lies in the range of 8–20, and can be readily controlled by the reaction time (to be discussed later in the part of growth mechanism). The typical Raman shift of the prepared sample is shown in Fig. 2e, and displays the strong and wide D-band at ~1354 cm^{-1} and G band at ~1590 cm^{-1}. It is difficult to observe the 2D band around 2700 cm^{-1}. This results in a small intensity ratio of 2D band to G band, which suggests that the prepared CNRs possess weak crystallinity and a lot of defects. The XRD pattern (Fig. 2f) shows a wide and weak peak at 25.1° and a strong Si (200) peak at 32.9°, indicating that a layered structure with the interlayer spacing of ~0.35 nm exists in the CNA. The interlayer spacing of the material can be established by Bragg's
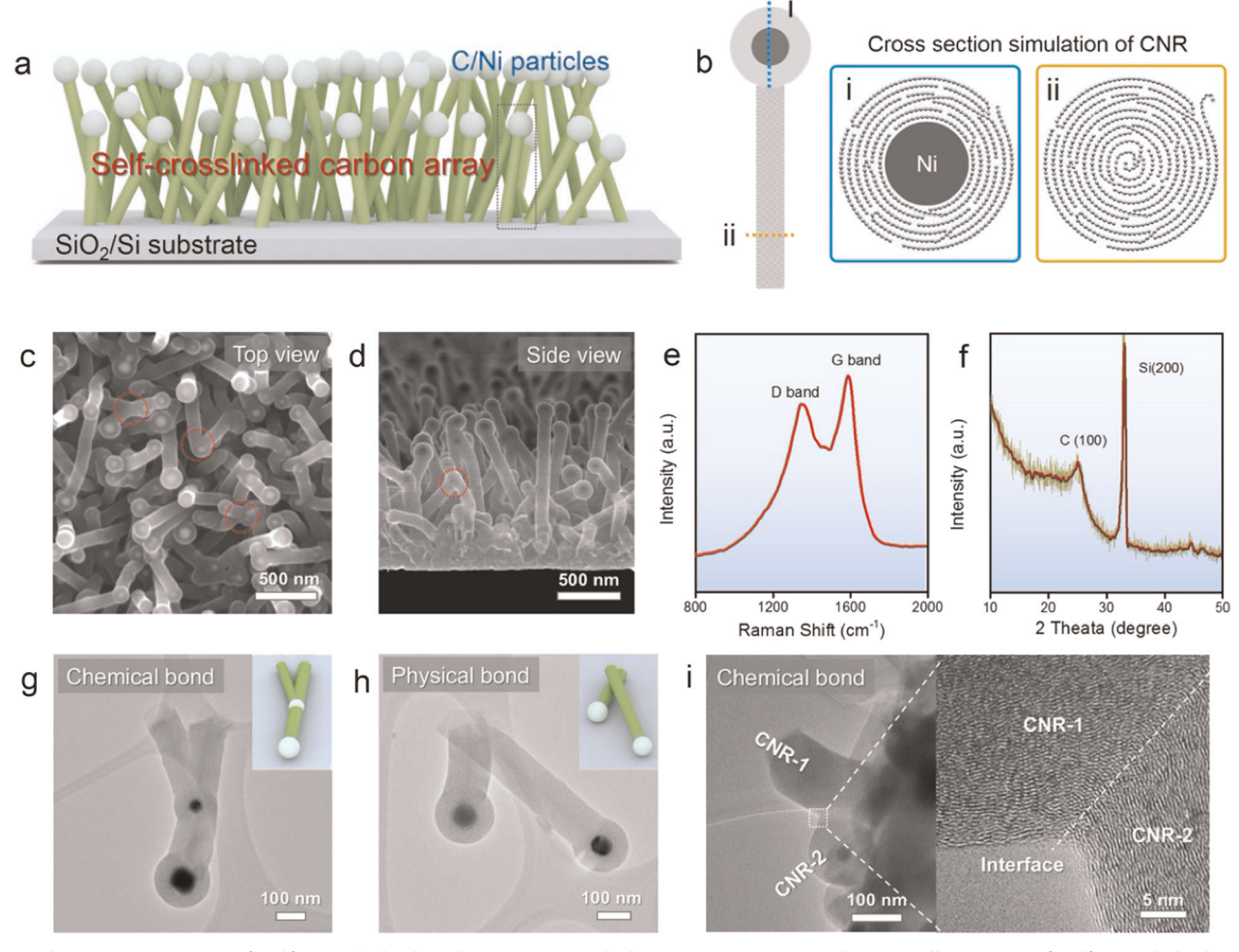
Fig. 2 Schematic structure of self-cross-linked carbon arrays and characterizations. a Schematic illustration of self-cross-linked carbon arrays. **b** The cross-section simulation of the CNR, suggesting that the individual unit of CNA is different than that of CNT and that it is an intermediate state between the CNT and carbon nanofiber. Top view (**c**) and side view (**d**) SEM images of self-cross-linked CA show the individual unit vertically aligned to the substrate and cross-linked to each other. The contact points between the individual units are both strong chemical bonds and physical stacking interactions. **e** A typical Raman shift of the sample shows the amount of defects that exist in the prepared CNA. **f** XRD pattern shows a wide and weak peak at 25.1°, which indicates a layered structure with the interlayer spacing of ~0.35 nm in CNA. **g, h, i** TEM images of CNRs connected with chemical bond (**g, h**) and physical stacking (**i**), respectively.

law, and its value is close to the interlayer spacing of graphite and multiwall CNTs[27–30]. The dashed circles in Fig. 2c, d indicate the CNA contains self-cross-linked points, which are strong chemical bonds. The TEM images (Fig. 2g–i) show that there are both chemical bond and physical stacking between the single CNA unit. Physical stacking will be played as switch under bend and strain, while chemical bond could be stretched to a certain extent. The switchable physical stacking could change the path of electron conduction, and results in changing the conductivity of 3D CNA film upon strain. Chemical bond is the strong contact point to make nanorods close-connected and cross-linked each other, which provides 3D CNA film with high structural stability. The cross-linked point is a chemical bond, which has lower contact resistance than physical stacking. Therefore, increasing the density of cross-linked points will enhance mechanical properties and reduce the resistivity of the whole film. We believe these self-cross-linked points and physical stacking will make the materials with novel mechanical and electrical properties, and promising in flexible sensor applications.

The growth mechanism (Fig. 3a) of CNA was proposed after investigation on the microstructures and growth process of CNA. To investigate the inner microstructures of as-prepared CNA by

TEM, the carbon nanorods on SiO2/Si substrate were scraped from the substrate and dispersed in ethanol solution. The solution was then dropped to a carbon-filmed copper grid and dried for TEM characterization. Figure 3b shows the typical TEM image of a single CNR. Notably, it is different from CNT with the tubular structure not observed from our carbon nanomaterial. The black region in Fig. 3b is the Ni catalyst, which is covered by the carbon layers. High-resolution TEM (HRTEM) image of the carbon layers on Ni catalyst (Supplementary Fig. S4, magnification of the white dashed box in Fig. 3b) shows the covered carbon layer has a thickness of ~43 nm (110–130 layers). The fingerprint-like structure suggests that the layered structure existed in carbon materials. We believe that these carbon layers suppressed the Ni catalyst and eliminated the growth of longer carbon nanorods, which is similar to the mechanism of the Ni catalyst growth of multi-walled carbon nanotubes[25,26]. Figure 3c presents the HRTEM images of the edge region of a carbon nanorod (magnification of the dark dashed box in Fig. 3b). The carbon layers can be clearly observed by the dark and white fingerprint lines, which have a layer spacing of ~0.36 nm that is close to, but slightly larger than, the interlayer spacing of graphite and carbon nanotube[29,30]. The carbon nanorod was made up of multiple carbon layers. The
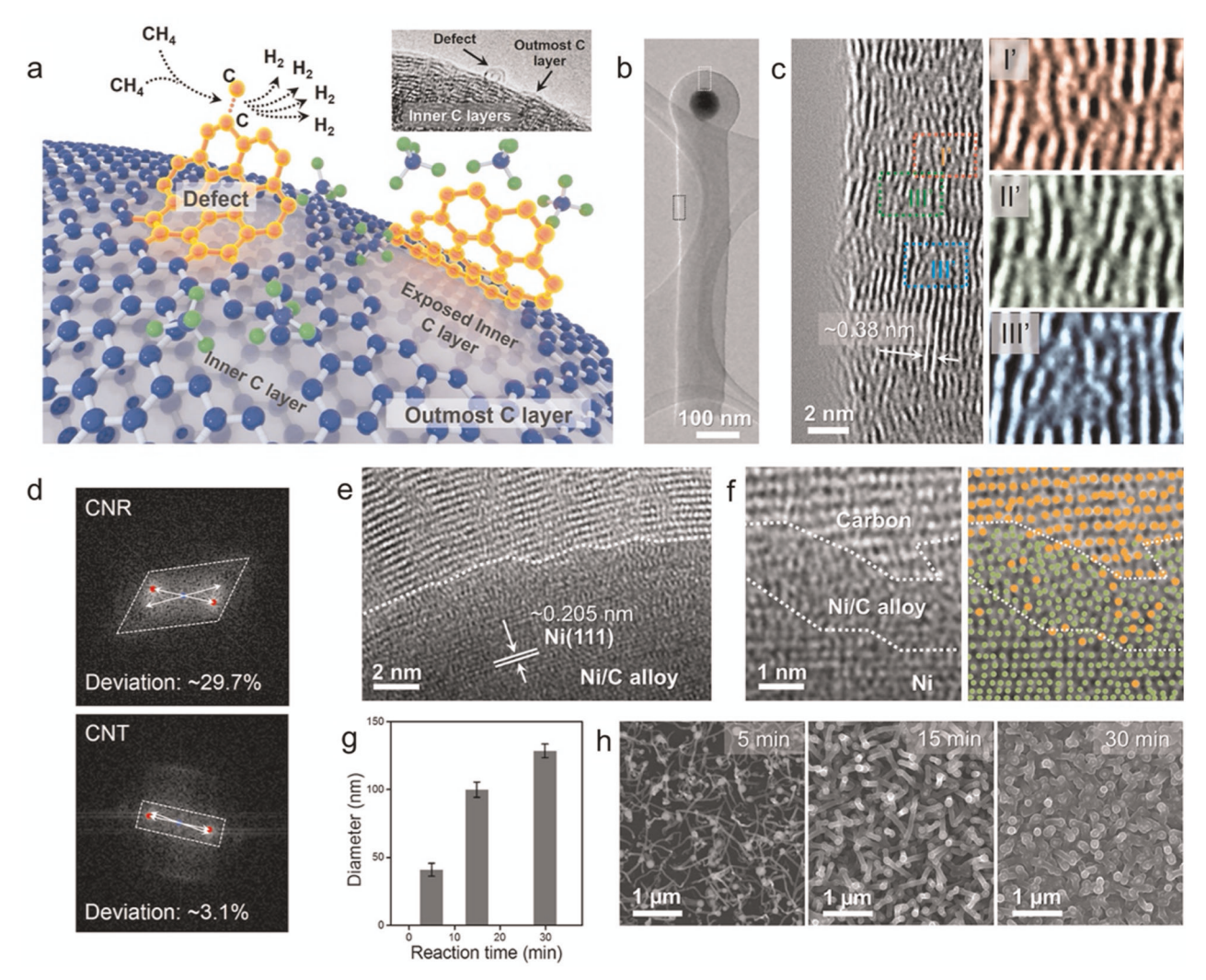
Fig. 3 Growth mechanism and TEM characterization of the individual CNA units. a Schematic illustration for growth mechanism of CNA. Inset: TEM images of CNA observed from the outside interface of individual units, which show the defects at the outmost carbon layers. **b** Low-magnification TEM image of a single-carbon nanorod shows the Ni catalyst located in the center of one terminal, and fully covered by the carbon layers. **c** High-resolution TEM images observed from the marked gray square in b. I', II', III' are magnified HRTEM images from the marked regions of **c**, respectively, indicating the discontinuous and crooked carbon layer stacking and the abundant defects. **d** Fast Fourier transform (FFT) patterns converted from HRTEM images of CNR and CNT indicate that the CNR have larger interlayer spacing deviation than CNT. **e, f** HRTEM images observed from the interface of the Ni catalyst and carbon layers. Right side of **f** shows re-structured simulation for the interface of Ni and carbon layers. The carbon layers are parallel to the Ni (111) lattice plane, suggesting that the carbon atoms were separated from alloy along the Ni (111) lattice plane in the growth process. **g** The diameter of the individual unit of the CNA with the reaction time. **h** SEM images of the materials synthesized by different reaction times.

discontinuous and crooked fingerprint lines in the HRTEM image indicates that each layer of the carbon nanorod is filled with the defects, as shown in Fig. 3c-I', II', and III'. Figure 3d presents fast Fourier transform (FFT) patterns converted from HRTEM images of CNR and CNT (Supplementary Fig. S5). The interlayer spacing deviations were established to 29.7% for CNR and 3.1% for CNT, which calculated by the deviation of FFT patterns. The interlayer spacing deviation of CNR is significantly larger than that of CNT, suggesting defects and lattice distortions in synthesized CNR nanomaterials, which are consistent with the results from Raman spectrum and HRTEM images. Therefore, the number of defects is one of the important characteristics for distinguishing the CNR from CNT. The abundant defects in the CNR may endow it with different kinds of mechanical and electrical properties, such as increased tensile strength and modified electron transport behavior because of the quasi-one-dimensional geometry[31,32].

Growth mechanism of carbon nanorod arrays

We employed CVD method with CH_4 gas as the carbon precursor and Ni catalyst to synthesize CNA at high temperatures and a dynamic change of pressure. Figure 3a schematically illustrated the growth mechanism of CNA. According to chemical thermodynamics, CH_4 will decompose into solid carbon and H_2 at high temperatures because the Gibbs free energy of solid carbon and H_2 are lower than that of CH_4 in the same environment. Previous research has demonstrated that the pyrolysis of CH_4 in a flow reactor (such as tube furnace) belongs to the first-order reaction, with the reaction rate constant and the activation energy being $\lg k(s^{-1}) = (13-18.6) \times 10^3/T$ and $E_a = 356$ kJ·mol^{-1}, respectively[33]. At the early stages of the high-temperature reaction, the CH_4 gas produces aromatic compounds which have higher molecular mass and lower Gibbs free energy. The Gibbs free energy of most aromatic compounds is lower than that of CH_4 at the temperature range of 1100–2000 °C[34]. As such, the compounds will gradually

thermo-decompose into carbon[35]. However, the pyrolysis mechanism of CH_4 in our experiment was different than that of the above process. The CH_4 gas directly decomposed into carbon and H_2 instead of aromatic compounds due to the relatively low reaction temperature (900 °C). As shown in Supplementary Fig. S6, the Gibbs free energy of CH_4 is lower than that of aromatic compounds at the temperature of 900 °C, suggesting that the aromatic compounds are thermodynamic nonequilibrium in this situation[34,36]. The 5-nm Ni catalyst film was heated to generate liquid Ni nanoparticles when the temperature reached 900 °C. Then, CH_4 gas was introduced into the tube furnace, which subsequently decomposed into carbon atoms, which was absorbed by the Ni catalyst to form Ni/C alloy. When the concentration of carbon exceeds the saturation concentration in Ni/C alloy, the carbon atoms separate from the Ni/C alloy to form solid carbon (Supplementary Fig. S7). The HRTEM images taken from the interface of the Ni catalyst and carbon layers are displayed in Fig. 3e, f. These images clearly show the carbon layers and the (111) lattice plane of the Ni catalyst. The carbon layers are almost parallel to the Ni (111) lattice plane, which suggests that the carbon atoms were separated from alloy along with the Ni (111) lattice plane, which is the same process in the growth of CNT

and graphene by the Ni catalyst[37–39]. Due to the weak hydrophilicity between the liquid Ni/C nanoparticles and the SiO_2/Si substrate, the liquid nanoparticles will lift off from the substrate by the synergistic effect of the saturated carbon nanorods. The defects in the carbon layers possess high chemical energy for the absorption of decomposed carbon atoms, and hence, act as the active site to grow carbon nanorods layer by layer. The defects bring about the stacking fault, and trigger a mass of defects in the final product (inset in Fig. 3a; Supplementary Fig. S7). We synthesized the CNR with different reaction times, and the results indicated that the average diameter of CNRs was significantly increased as we prolonged the reaction time, while the length of CNRs was not changed (Fig. 3g, h). This phenomenon is different than in the growth of CNTs, where the length of the nanorods were changed with the reaction time, but the diameter was determined by the size of the catalyst[23,25,40]. This result further demonstrates the defects in the outmost carbon layers that are crucial in the growth of CNRs.

Carbon nanorod arrays for bendable and vibration sensors

The prepared CNA was transferred to flexible substrates such as PET for resistance-type sensors. As shown in Fig. 4a, we employed
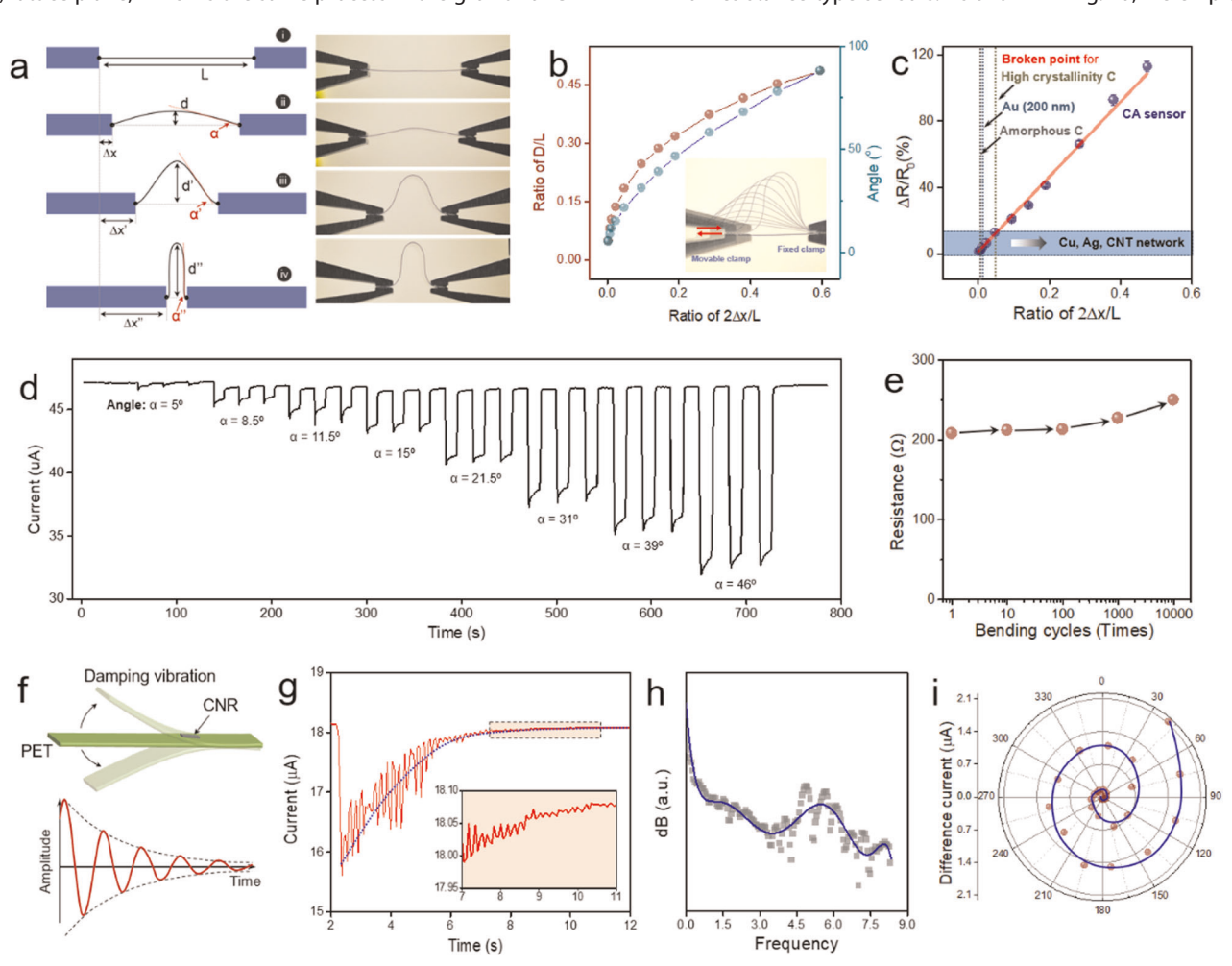

Fig. 4 CAN-based flexible sensors for the detection of flexion and low frequency vibrations. a Schematic illustrations and optical graphs of PET substrate with CNA materials under different bending conditions. **b** The ratio of d/L (the derived height over device size) and bendable angles with the ratio of 2Δx/L (the step distance over device size). Inset shows the overlapped optical graphs of device with different bending conditions. **c** The sensitivity of device with various materials under different bending conditions. **d** Real-time I–t curve of CNA device with various bending circles. **e** The resistances of device under different bend conditions. **f** Schematic illustration of damping vibrations generated by PET substrate, where the CNA-based sensor was set on its surface. **g** Real-time current response of CNA-based sensors to damping vibrations. **h** The real-time I–t curve was processed by fast Fourier transform (FFT), which indicates that the dominant frequency of this damping vibration is ~5.5 Hz. **i** The polar coordinate of the current intensity changes.

two clamps driven by the high-resolution stepping motor to clamp down the device with varying step distances (Δx). The bendable angle (α) and derived height (d) were used to quantify the bend behavior, where α and d gradually increased when the bending intensified as we are increasing the step (from i to iv). In order to eliminate the size effect of our devices, we used the ratio of derived height (d) over device length (L) to describe the bending behavior. When the step distance was linearly increased, the ratio of d/L and bend angle (α) showed similar nonlinear behaviors, where the ratio of d/L trend to the value of 0.5 and the bend angle (α) trend to 90°, respectively (Fig. 4b). We measured the resistance change of the device using different bend angles from 5° to 88° achieved by bending with the ratio of d/L from 0.002 to 0.595, corresponding to the derived height from 2 to 20 mm. The resistance sensitivity S is defined as the normalized resistance change, $S = (R - R_0)/R_0 \times 100\% = \Delta R/R_0 \times 100\%$, where R is the resistance of the device when bended and R_0 is the resistance when the device is relaxed. The sensitivity of the device at different bend angles and the real-time resistance sensitivity are displayed in Fig. 4c, d, respectively. Notably, the resistance sensitivity of the CNA device increased gradually as the bending increased, and it shows a linear relationship with the ratio of 2Δx/L. The real-time resistance sensitivity curve indicates that the CNA device repeatedly gave a fast response to the external stimulation of bending. More importantly, the signals recovered promptly (<1 s) to the original baseline value upon the relaxing of the device. We compared the performance of our CNA-based device with solid film (such as amorphous carbon film, high crystallinity carbon film), and 2D network films (Ag network, and CNT network)-based devices (Fig. 4c)[19,41]. It can be seen that the 3D CNA-based device has the highest sensitivity, the best stability, and reproducibility, as well as the largest tolerable detection range as compared to the other devices. The performance of CNA devices beyond that of almost network structures and solid films in sensitivity and detection range, respectively (Fig. 1b). To investigate the stability of CNA device, we bent it more than 10,000 times, with a bend angle of ~45° and a duration of ~8.3 h (3 s per cycle). As shown in Fig. 4e, our device showed good stability, with only a minor resistance change (~20%). The device still presents good performance when bent with 10,000 times. To investigate the changes in the microstructure of materials, we employed the optical microscopy and homemade moveable stage for the in situ characterization of materials upon bending (Supplementary Fig. S8). The CNA film presents better mechanical property than a solid film. When bending to 90°, few cracks (with the density of <1 crack/100 μm) were observed in CNA film, while a mass of cracks (with the density of ~15 cracks/100 μm) existed in bended solid films. Typically, the material with low flexural stiffness could be bend easily. Flexural stiffness can be estimated as equation[42]: $D = Eh^3/12(1 - v^2)$, where E denotes the elastic modulus, h and v represent the thickness and Poisson's ratio of materials, respectively. It is noted that 3D self-cross-linked materials have lower elastic modulus than solid films due to their specific geometry. Therefore, we believe the self-cross-linked points and vertically aligned individual nanorod unit in 3D CNA films reduced elastic modulus, which avoids the mechanical cracking when bending, and making the CNA-based flexible device possess superior structural stability to a solid film.

Our CNA-based device can be used to act as a mechanical sensor to detect vibrations. As an example, we generated damping vibration by bending and freely relaxing the device on a PET substrate, wherein one of the terminals was fixed and the other was kept free (Fig. 4f). The damping vibration test can be simulated on the PET substrate due to its big Young's modulus (~2–4 GPa) and suitable elasticity. As such, the up and down "spring-like" movement of the PET substrate-induced strain and pressure to the CNA material. The real-time current changes of the device were recorded throughout the entire damping vibration

process, as displayed in Fig. 4g. When the device was bent downward, the current significantly decreased. Subsequently, the current fluctuated in response to the vibration, and eventually, as the damping vibration stopped, returned to the original baseline. The real-time I–t curve depicted in Fig. 4g was processed by the fast Fourier transform (FFT), and the frequency data obtained is shown in Fig. 4h. The fitted curve (blue line in Fig. 4h) indicates that the dominant frequency of the damping vibration process is ~5.5 Hz. Our CNA-based flexible sensor presents high sensitivity for detection and recording the damping vibration with a frequency of ~5.5 Hz. In Fig. 4i, we established the polar coordinate to describe the current intensity changes of the device, where the average half maximum was defined as the current intensity and 2 s was defined as one period of polar coordinate. The results showed that the current intensity spirally decreased to the center of the coordinate, which denoted the current base point of the device. The current intensity change in this polar coordinate shows similar behavior to the traditional amplitude change in the damping vibration, suggesting that the CNA-based flexible device is capable of the detection of damping vibration.

Carbon array-based flexible sensors for monitoring the Parkinsonian tremor

The human body has a lot of vibration information, named body tremors, which typically have a frequency in the range of 6–50 Hz[43,44]. These tremors are signs of body conditions and the disease, such as rest tremor, which is a symptom of neurological disorder. We have demonstrated that the CNA-based flexible sensors can be used in the detection of vibration with a frequency ranged in 5–20 Hz, which is close to the frequency of body tremors. Parkinsonian tremor shows pill-rolling action of the thumb, and is often a precursor to Parkinson's disease (Fig. 5a). High-precision commercial vibration sensor on the handphone as a referenced sensor for evaluation. CNA flexible device was attached to the human hand near the adductor pollicis, and an iPhone 6 was used as a referenced sensor (Fig. 5a, inset of Fig. 5b). We simulated the Parkinsonian tremor by vibrating the hand and thumb. The real-time I–t curve of the CNA device and the real-time signal from the iPhone 6 sensor fully recorded the simulated tremors, as displayed in Fig. 5b. Both signals were processed by short-time Fourier transform (STFT), and the processed image of time and frequency of the CNA device has a high concordance with the reference sensor of the iPhone 6 (Fig. 5c). Due to the severe body tremors, the handwriting of Parkinsonian is different than that from normal persons (Fig. 5d)[45]. Figure 5e shows the real-time response of CNA-based flexible sensors on monitoring the handwriting with and without tremors, suggests the sensor is sensitive to hand tremors when writing and capable of recording of handwriting. The sensitivity of our flexion sensor close to 10%, which is higher than the conductive liquid-based strain sensor (~5%) performed in the detection of human tremor[22]. Frequency spectrograms (Fig. 5f) of the flexible sensor in the detection of hand tremors indicate that there are two frequencies vibrations of ~5.5 and ~11.0 Hz, respectively. We detected the handwriting on the word of "Parkinsonism" with (red curve) and without (blue curve) simulated hands tremors by CNA flexible sensors (Fig. 5g). Due to the high stability of devices, their applications in monitoring Parkinsonian tremor could be continued in a long time. The result shows CNA-based flexible sensor possesses high sensitivity and good reliability in monitoring the simulated Parkinsonian's tremors and handwriting. Notably, the low working voltage of <1 V makes a device with low-power consumption, which is important for wearable electronic applications. The performance of low-cost CNA flexible sensor is comparable with the referenced high-cost commercial sensor that produced by micro-manufacture technology. Therefore, the CNA-based flexible
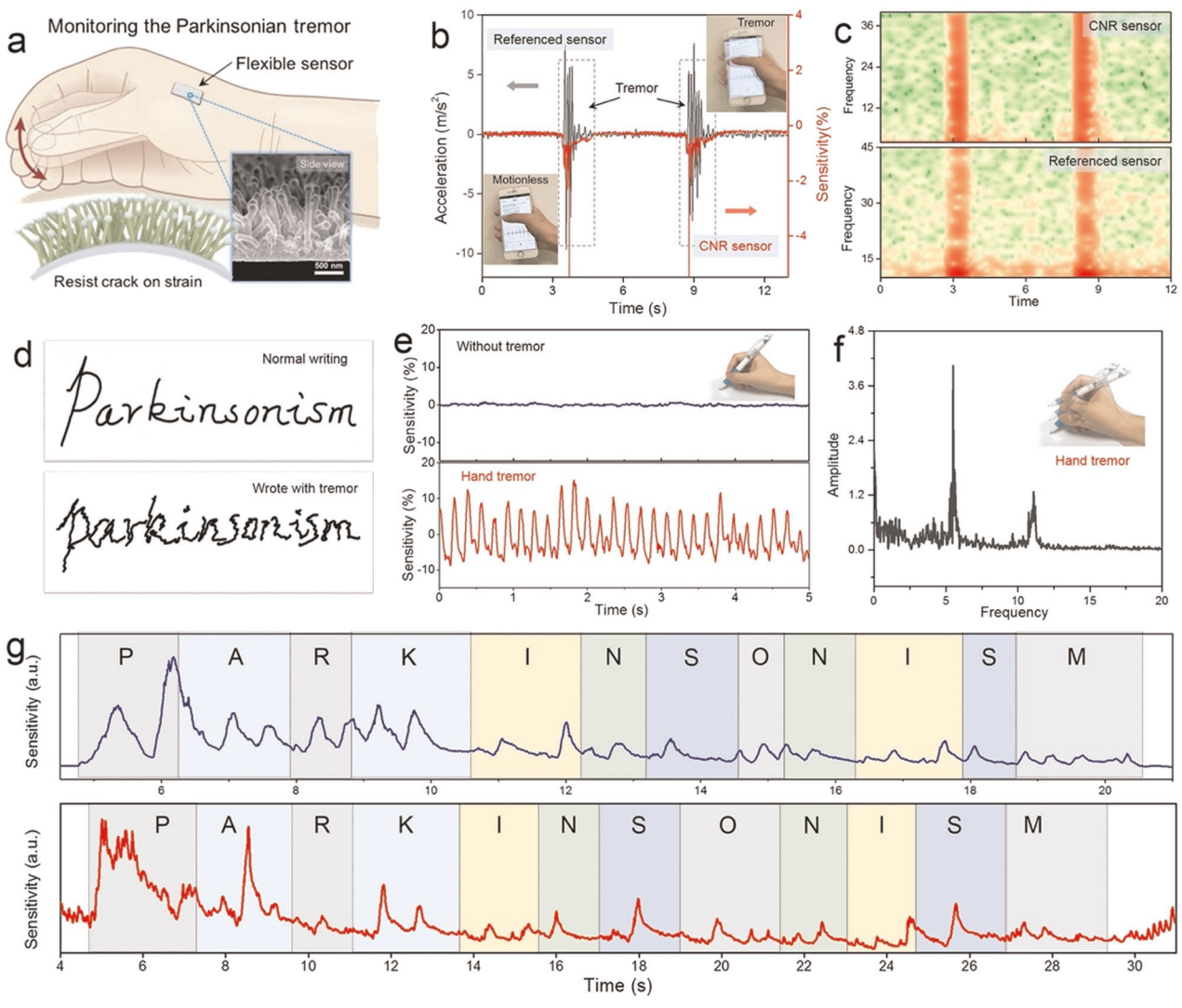
Fig. 5 **Monitoring the Parkinsonian tremor by CNA-based flexion sensors. a** Schematic illustrations of monitoring Parkinsonian tremors by CNA-based flexible sensor. **b** The CNA-based flexible sensor and reference sensor of the iPhone 6 were placed on the human hand to monitor the simulated Parkinsonian tremors. Real-time response of CNA-based flexible sensor (red curve) and reference sensor (black curve) recorded the hand tremors. **c** Short-time Fourier transform (STFT) processed signals of our flexible sensor and referenced sensor, indicate that the performance of cost-effective CNA-based flexible sensor is comparable with the reference commercial sensor. **d** Chirographies of normal writing and writing with tremor. **e** Real-time response of CNA-based flexible sensors on monitoring the handwriting with and without tremors, suggests the sensor is sensitivity to hand tremors when writing. **f** Frequency spectrograms of flexible sensor in detection of hand tremors, indicts that there are two frequencies vibrations of ~5.5 and ~11.0 Hz, respectively. **g** Real-time detection of handwriting on "Parkinsonism" with (red curve) and without (blue curve) simulated hands tremors.

sensor paves the way for low-cost, flexible health sensors that can be used for health monitoring.

DISCUSSION

Flexible sensors were revolutionary techniques for health monitoring. The technique will bring a significant change of the conventional diagnosis in clinical practice toward portable, wearable, remote, and timely. In this study, we have demonstrated CNA-based flexible sensors capable of monitoring multiple mechanical related physiological signals, such as wrist pulse, heart rate, respiratory rate, and rest tremors (Supplementary Fig. S9; Fig. 5). These flexible sensors could be used to collect personal health-related information, including REM sleeping, heart rate/ blood pressure, rest tremor, and body motion, then analyzed by deep neural networks of machine learning to extract characteristic features of Parkinsonian. The body condition and therapeutic method will be feedback to the hospital and patient for further

treatments. In this process, the physician could be freed from diagnosis and pay more attention to medical treatments. We believe the combination of flexible healthcare sensors and artificial intelligence deep-learning techniques for doctorless disease diagnosis.

In summary, we have prepared 3D self-cross-linked CNA and demonstrated its applications in flexible sensing electronics. We find that this novel carbon nanomaterial is far more superior to 2D networks and solid thin films in the application as flexible electronics, and shows high performance in the detection of flexion and low-frequency vibrations (~6 Hz). These include high sensitivity, low-power consumption as well as good stability and reliability. These attributes enable the 3D self-cross-linked CNA to be a promising tool in the pre-diagnosis of Parkinson's disease by tracking the diagnostic rest tremors. This study paves the way for the wearable health-monitoring system, and seeks to propel the traditional disease diagnosis for Parkinson's disease toward cost-effective telemedicine.

METHODS

Synthesis of self-cross-linked carbon arrays and characterization

The CVD method with CH_4 precursor and Ni catalyst were employed to synthesize of self-cross-linked carbon arrays. First, the 5-nm Ni catalyst on SiO_2/Si substrate was fabricated by E-beam deposition with the working voltage of ~4.99 kV and the current of ~90 mA. The micro-patterned Ni catalyst can be achieved by the traditional photolithography process. Then, the prepared SiO_2/Si substrate with 5-nm Ni catalyst was set into the center of the quartz tube furnace. For flushing and removing the residual air in the tube, the H_2 gas was inlet into it for 15 min. The mechanical pump was linked to the quartz tube for pumping until the pressure down to ~1.5 mBar. Then, the furnace was heated to 900° and kept for 15 min at 900°. In the heat preservation process at 900°, the gas vent keeps closed, and the pure CH_4 gas was inlet into the furnace with a strictly controlled flow rate of 10 sccm. In this process, the pressure was gradually increased from ~1.5 mBar to ~155 mBar in 15 min. After that, the CH_4 gas was switched to pure H_2, and the furnace was cooling down to room temperature. Finally, the carbon nanorods array was grown onto SiO_2/Si substrate, and followed geometries of Ni catalysts. The prepared samples were characterized by SEM (JEOL 6340), TEM (JEOL 2010HR, JEOL 2100F), XRD (Bruker D8 Advance), and Raman (WITec alpha300 RAS Raman system).

Fabrication of CA-based flexible sensing electronics and performance measurements

The prepared CA was transferred to target flexible substrate such as PET and PDMS for device fabrication. The CA can be lift off from SiO_2/Si substrate by etching SiO_2 layer using HF solution. We cut the edge of prepared CA materials on SiO_2/Si substrate, make sure the SiO_2 layer bared to the environment, and immersed it to HF solution for ~12 h. The SiO_2 layer will be etched from the edge to the center of materials. Finally, the CA floated onto the surface of HF solution. The PET film and PDMS film were used to transfer the floated CA by immersing them in HF solution. Then, the CA with PET (or PDMS) was rinsed by DI water several times for removing the residual HF. The Cu wires with Ag paste were connected to each terminal of CA materials to form resistance sensors. The semiconductor device analyzer (Agilent 1500B) and Lab VIEW-controlled digital source meter (Keithley 2450) were used to measure the resistance change of devices in real-time. The homemade linear stepper stage with the resolution of 10 μm was used to load the bending to the device, and the digital camera was employed to measure the bendable angles and derived heights.

DATA AVAILABILITY

The data sets generated during and/or analyzed during the current study are available from the corresponding author on reasonable request.

REFERENCES

1. Xu, J. et al. Highly stretchable polymer semiconductor films through the nano-confinement effect. *Science* **355**, 59–64 (2017).
2. Wu, W., Wen, X. & Wang, Z. L. Taxel-addressable matrix of vertical-nanowire piezotronic transistors for active and adaptive tactile imaging. *Science* **340**, 952–957 (2013).
3. Kim, D. H. et al. Electronic sensor and actuator webs for large-area complex geometry cardiac mapping and therapy. *Proc. Natl Acad. Sci. USA* **109**, 19910–19915 (2012).
4. Wang, S. et al. Skin electronics from scalable fabrication of an intrinsically stretchable transistor array. *Nature* **555**, 83–88 (2018).
5. Wang, C. et al. User-interactive electronic skin for instantaneous pressure visualization. *Nat. Mater.* **12**, 899–904 (2013).
6. Someya, T. et al. A large-area, flexible pressure sensor matrix with organic field-effect transistors for artificial skin applications. *Proc. Natl Acad. Sci. USA* **101**, 9966–9970 (2004).
7. Jiang, H. et al. Finite deformation mechanics in buckled thin films on compliant supports. *Proc. Natl Acad. Sci. USA* **104**, 15607–15612 (2007).
8. Wang, X., Liu, Z. & Zhang, T. Flexible sensing electronics for wearable/attachable health monitoring. *Small* **13**, 1602790 (2017).
9. Chortos, A. & Bao, Z. Skin-inspired electronic devices. *Mater. Today* **17**, 321–331 (2014).
10. Yao, S. & Zhu, Y. Wearable multifunctional sensors using printed stretchable conductors made of silver nanowires. *Nanoscale* **6**, 2345–2352 (2014).
11. Cao, Q. & Rogers, J. A. Ultrathin films of single-walled carbon nanotubes for electronics and sensors: a review of fundamental and applied aspects. *Adv. Mater.* **21**, 29–53 (2009).
12. Jiang, K., Li, Q. & Fan, S. Nanotechnology: spinning continuous carbon nanotube yarns. *Nature* **419**, 801–801 (2002).
13. Krasheninnikov, A. V., Nordlund, K., Keinonen, J. & Banhart, F. Ion-irradiation-induced welding of carbon nanotubes. *Phys. Rev. B* **66**, 245403 (2002).
14. Garnett, E. C. et al. Self-limited plasmonic welding of silver nanowire junctions. *Nat. Mater.* **11**, 241–249 (2012).
15. Hirayama, H., Kawamoto, Y., Ohshima, Y. & Takayanagi, K. Nanospot welding of carbon nanotubes. *Appl. Phys. Lett.* **79**, 1169–1171 (2001).
16. Gu, Y. et al. Flexible electronic eardrum. *Nano Res.* **10**, 2683–2691 (2017).
17. Wang, X., Gu, Y., Xiong, Z., Cui, Z. & Zhang, T. Silk-molded flexible, ultrasensitive, and highly stable electronic skin for monitoring human physiological signals. *Adv. Mater.* **26**, 1336–1342 (2014).
18. Wang, X., Xiong, Z., Liu, Z. & Zhang, T. Exfoliation at the liquid/air interface to assemble reduced graphene oxide ultrathin films for a flexible noncontact sensing device. *Adv. Mater.* **27**, 1370–1375 (2015).
19. Lipomi, D. J. et al. Skin-like pressure and strain sensors based on transparent elastic films of carbon nanotubes. *Nat. Nanotechnol.* **6**, 788–792 (2011).
20. Trung, T. Q. & Lee, N. E. Flexible and stretchable physical sensor integrated platforms for wearable human-activity monitoringand personal healthcare. *Adv. Mater.* **28**, 4338–4372 (2016).
21. Tee, B. C.-K. et al. A skin-inspired organic digital mechanoreceptor. *Science* **350**, 313–316 (2015).
22. Guan, L. et al. Stretchable-fiber-confined wetting conductive liquids as wearable human health monitors. *Adv. Funct. Mater.* **26**, 4511–4517 (2016).
23. Li, Y. M. et al. Growth of single-walled carbon nanotubes from discrete catalytic nanoparticles of various sizes. *J. Phys. Chem. B* **105**, 11424–11431 (2001).
24. Hayashi, T. et al. Smallest freestanding single-walled carbon nanotube. *Nano Lett.* **3**, 887–889 (2003).
25. Dupuis, A. C. The catalyst in the CCVD of carbon nanotubes - a review. *Prog. Mater. Sci.* **50**, 929–961 (2005).
26. Xu, F., Liu, X. & Tse, S. D. Synthesis of carbon nanotubes on metal alloy substrates with voltage bias in methane inverse diffusion flames. *Carbon* **44**, 570–577 (2006).
27. Andrews, R., Jacques, D., Qian, D. & Dickey, E. C. Purification and structural annealing of multiwalled carbon nanotubes at graphitization temperatures. *Carbon* **39**, 1681–1687 (2001).
28. Hamwi, A., Alvergnat, H., Bonnamy, S. & Béguin, F. Fluorination of carbon nanotubes. *Carbon* **35**, 723–728 (1997).
29. Bacon, B. G. E. The interlayer spacing of graphite. *Acta Cryst.* **4**, 558–561 (1951).
30. Saito, Y., Yoshikawa, T., Bandow, S., Tomita, M. & Hayashi, T. Interlayer spacings in carbon nanotubes. *Phys. Rev. B* **48**, 1907–1909 (1993).
31. Krasheninnikov, A. V. & Banhart, F. Engineering of nanostructured carbon materials with electron or ion beams. *Nat. Mater.* **6**, 723–733 (2007).
32. Astrom, J. A., Krasheninnikov, A. V. & Nordlund, K. Carbon nanotube mats and fibers with irradiation-improved mechanical characteristics: a theoretical model. *Phys. Rev. Lett.* **93**, 215503 (2004).
33. Palmer, H. B., Lahaye, J. & Hou, K. C. Kinetics and mechanism of the thermal decomposition of methane in a flow system. *J. Phys. Chem.* **72**, 348–353 (1968).
34. Yuliati, L. & Yoshida, H. Photocatalytic conversion of methane. *Chem. Soc. Rev.* **37**, 1592–1602 (2008).
35. Chen, C. J., Back, M. H. & Back, R. A. The thermal decomposition of methane. II. Secondary reactions, autocatalysis and carbon formation; non-Arrhenius behaviour in the reaction of CH3 with ethane. *Can. J. Chem.* **54**, 3175–3184 (1976).
36. Tang, P., Zhu, Q., Wu, Z. & Ma, D. Methane activation: the past and future. *Energy Environ. Sci.* **7**, 2580 (2014).
37. Weatherup, R. S. et al. Introducing carbon diffusion barriers for uniform, high-quality graphene growth from solid sources. *Nano Lett.* **13**, 4624–4631 (2013).
38. Wang, X. et al. Programmable high crystallinity carbon patterns. *2D Mater.* **4**, 025011 (2017).
39. Klinke, C., Bonard, J.-M. & Kern, K. Comparative study of the catalytic growth of patterned carbon nanotube films. *Sur. Sci.* **492**, 195–201 (2001).
40. Cheung, C. L., Kurtz, A., Park, H. & Lieber, C. M. Diameter-controlled synthesis of carbon nanotubes. *J. Phys. Chem. B* **106**, 2429–2433 (2002).
41. Xu, F. & Zhu, Y. Highly conductive and stretchable silver nanowire conductors. *Adv. Mater.* **24**, 5117–5122 (2012).
42. Lacour, S. P., Courtine, G. & Guck, J. Materials and technologies for soft implantable neuroprostheses. *Nat. Rev. Mater.* **1**, 1–14 (2016).

43. Sonza, A., Robinson, C. C., Achaval, M. & Zaro, M. A. Whole body vibration at different exposure frequencies: infrared thermography and physiological effects. *ScientificWorldJournal* **2015**, 452657 (2015).
44. McAuley, J. H., Rothwell, J. C. & Marsden, C. D. Frequency peaks of tremor, muscle vibration and electromyographic activity at 10 Hz, 20 Hz and 40 Hz during human finger muscle contraction may reflect rhythmicities of central neural firing. *Exp. Brain Res.* **114**, 525–541 (1997).
45. Gemmert, A. W. A. V., Teulings, H. L., Contreras-Vidal, J. L. & Stelmach, G. E. Parkinsons disease and the control of size and speed in handwriting. *Neuropsychologia* **37**, 685–694 (1999).

ACKNOWLEDGEMENTS

AUTHOR CONTRIBUTIONS

Z.L., T.Z., and X.W. conceived and designed the experiments. X.W., M.M., and L.Z. performed the growth of materials. W.F., L.Z., and G.G. carried out the TEM characterizations. W.F. drawn all of the schematic illustrations. H.W. and X.W. conducted Raman measurements. X. W., M.M., and Y.G. fabricated the devices and studied their performance. X.W., Z.L., and T.Z. co-wrote the paper. M.M. polished the paper language. All authors contributed to the results analysis and discussions.

COMPETING INTERESTS

The authors declare no competing interests.

ADDITIONAL INFORMATION

Publisher's note Springer Nature remains neutral with regard to jurisdictional claims in published maps and institutional affiliations.